Soft Matter

Elastohydrodynamic propulsion of a filament magnetically driven at both ends

Journal:	*Soft Matter*
Manuscript ID	SM-ART-04-2023-000464.R1
Article Type:	Paper
Date Submitted by the Author:	18-Aug-2023
Complete List of Authors:	Gürbüz, Ali; Santa Clara University Qin, Ke; Santa Clara University, Abbott, Jake; University of Utah Pak, On Shun; Santa Clara University, Department of Mechanical Engineering

Soft Matter

ARTICLE TYPE

Cite this: DOI: 00.0000/xxxxxxxxxx

Elastohydrodynamic propulsion of a filament magnetically driven at both ends†

Ali Gürbüz[a], Ke Qin[a], Jake J. Abbott*[b], and On Shun Pak*[a,c]

Received Date
Accepted Date

DOI: 00.0000/xxxxxxxxxx

The elastohydrodynamic interaction between an elastic filament and its surrounding fluid has been exploited to develop the first microswimmers. These flexible microswimmers are typically actuated magnetically at one end and their propulsion behavior is relatively well understood. In this work, we move beyond the traditional single-end actuation setup and explore the propulsion characteristics of an elastic filament driven by magnetic torques at both ends. We report the emergence of new modes of propulsion behaviors in different physical regimes, depending on the balance of elastic and viscous forces as well as the arrangement of the magnetic moments at the filament ends. In particular, under the same magnetic actuation, a filament driven at both ends can propel either forward or backward depending on its relative stiffness. Moreover, this new backward propulsion mode can generate a magnitude of propulsion that is unattainable by the traditional single-end actuation setup. We characterize these new propulsion behaviors and provide some physical insights into how they emerge from the complex interplay between viscous and elastic forces and magnetic actuation in various configurations. Taken together, these findings could guide the development of soft microrobots with enhanced propulsion performance and maneuverability for future biomedical applications.

1 Introduction

Due to their potential use in biomedical applications such as drug delivery and microsurgery[1–3], the development of swimming microrobots that can propel through the microscopic world like living microorganisms has attracted considerable attention[4–9]. The locomotion of these microswimmers typically occurs at a very low Reynolds number (Re): consider a swimmer with a characteristic size $L = 10$ μm propelling through a fluid with a kinematic viscosity $\nu = 1$ mm^2/s at a typical speed $U = 10$ μm/s, we have $\mathrm{Re} = UL/\nu = 10^{-4}$, indicating a dominance of viscous forces over inertial forces in the fluid. The absence of inertia at the microscale imposes a fundamental challenge to locomotion at low Re for microorganisms and artificial microswimmers[10–13]. Purcell's scallop theorem[14] states that any reciprocal motion (*i.e.,* sequence of motions with time-reversal symmetry) cannot generate net propulsion without inertia. This constraint renders some common macroscopic swimming strategies such as rigid flapping motion ineffective for locomotion at low Re.

Microorganisms have evolved diverse strategies to swim in their microscopic world. Some eukaryotic cells such as spermatozoa propel themselves by beating their hair-like structures that resemble elastic rods, known as flagella[10,11]. The beating motion is generated by the action of molecular motors within the flagellum[15,16]. The flexibility of the flagellum enables the propagation of a bending wave to break the time-reversal invariance and generate propulsion. This strategy, inspired by biological systems and based on the elastohydrodynamic interaction between an elastic structure and its surrounding fluid, has been utilized to develop the first artificial microswimmers[8,9,17–21]. Without molecular motors like those in microorganisms, the elastic body of artificial microswimmers instead are typically actuated with magnetic materials concentrated at one end[18–21] or distributed along the body[17,22–25] under external magnetic fields. The magnetic material attempting to align with oscillating magnetic fields then drives the elastic deformation of the filament, generating propulsion as a result of the elastohydrodynamic response.

Previous analyses have elucidated the fundamental propulsion behavior of an elastic filament that is driven by end actuation, such as torque, lateral displacement, and angular displacement at one end[19,27–34], which share some general features: a relatively stiff filament primarily undergoes reciprocal motion, resulting in negligible propulsive thrust as constrained by Purcell's scal-

[a] Department of Mechanical Engineering, Santa Clara University, Santa Clara, CA 95053, USA. Email: opak@scu.edu
[b] Department of Mechanical Engineering and the Robotics Center, University of Utah, Salt Lake City, UT 84112, USA. Email: jake.abbott@utah.edu
[c] Department of Applied Mathematics, Santa Clara University, Santa Clara, CA 95053, USA.

† Electronic Supplementary Information (ESI) available. See DOI: 10.1039/cXsm00000x/

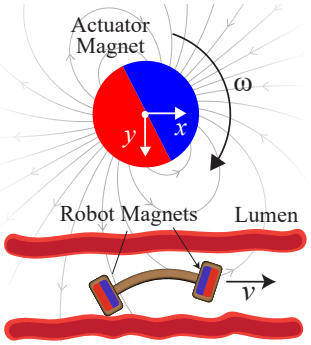

Fig. 1 A soft endoluminal robot comprises a compliant continuum structure with two embedded magnets of opposite polarity. Its locomotion is actuated by an external magnetic field. The soft robot can travel through lumens of the body for potential biomedical applications. Reproduced with permission [26]. Copyright 2020, IEEE.

lop theorem. With sufficient flexibility, the deformations along the filament give rise to a propulsive thrust directed towards its actuated end. However, an excessively flexible filament has reduced propulsion because its deformation becomes more localized around the actuated end. Maximizing propulsion performance requires achieving an optimal balance between viscous and elastic forces, which are influenced by the bending rigidity of the filament, the viscosity of the surrounding fluid, and the frequency of actuation at the filament end. These general characteristics of elastohydrodynamic propulsion with end actuation are well characterized in terms of relevant dimensionless groups (see more details in §2 and §3 below). Other studies have also examined how variable bending stiffness [35,36], intrinsic curvature [37,38], non-Newtonian rheology [39–42], and interactions of multiple filaments [43–45] impact the propulsion performance of flexible microswimmers.

More recently, researchers have explored the use of a two-magnet concept in enabling crawling locomotion of soft robots in natural lumens of the human body [26,46]. These endoluminal soft robots comprise an elastic body attached with two permanent magnets with opposite polarity at its ends (Fig. 1). Under a rotating magnetic dipole field, these robots develop inchworm-link crawling gaits. Inspired by this two-magnet concept, we move beyond the traditional single-magnet arrangement in microswimmer and explore the design space with the two-magnet concept applied to elastohydrodynamic propulsion in a fluid medium. Specifically, we pose the following questions: Compared to the traditional single-end actuation setup, what is the effect on propulsion characteristics when magnetic actuation is applied at both ends of an elastic filament? Can the additional magnetic moment be exploited to enhance propulsion? How do the polarity and relative strength of the magnetic moments at the filament ends impact the resulting propulsion performance? In this work, we consider a minimal model consisting of an elastic filament driven by point magnetic torques at its two ends to address these fundamental questions. Our findings reveal new propulsion behaviors that were previously not observed in the traditional single-end actuation setup. The idealized problem setup allows us to gain physical insights into how these new propulsion behaviors emerge from the complex interplay between viscous and elastic forces and magnetic actuation in various configurations.

The paper is organized as follows. In §2, we describe the elastohydrodynamic model and magnetic actuation considered in our model problem. The problem is non-dimensionalized to identify relevant dimensionless groups. We then present results on the propulsion performance as a function of relevant dimensionless groups for elastic filaments driven by magnetic moments with the same (§3A) and opposite (§3B) polarities. In particular, we characterize and discuss in detail new modes of motion unique to the two-magnet setup in different physical regimes. In §4, we conclude this work with remarks on its limitations and several potential directions for subsequent investigations.

2 Problem Formulation

2.1 Elastohydrodynamics

We consider the motion of an elastic filament of radius a and length L in a viscous fluid. The position vector of a point of the filament neutral line is denoted as $\mathbf{x}(s,t) = x(s,t)\mathbf{e}_x + y(s,t)\mathbf{e}_y$, where $s \in [0,L]$ is the arclength along the filament and t is time. We assume the filament to be slender ($a \ll L$) and apply the resistive force theory [47,48] for slender bodies to describe the hydrodynamic force density along the filament as

$$\mathbf{f}^h = -(\xi_\perp \mathbf{nn} + \xi_\parallel \mathbf{tt}) \cdot \mathbf{u}, \tag{1}$$

where $\mathbf{u} = \mathbf{x}_t$ is the local velocity, and $\xi_\parallel = 2\pi\mu/[\ln(L/a) - 1/2]$ and $\xi_\perp = 4\pi\mu/[\ln(L/a) + 1/2]$ are, respectively, the resistive coefficients in the tangential and normal directions in a fluid of dynamic viscosity μ.

To model the fluid-structure interaction, we consider a framework based on a multi-link discretization of the elastic filament [41,49–51]. The filament is discretized by a chain of N rigid links of equal length $\ell = L/N$, which are serially connected by $N-1$ torsional springs with a spring constant k. For the i-th link, the position vector of its left end is denoted as $\mathbf{x}_i = x_i\mathbf{e}_x + y_i\mathbf{e}_y$. The unit tangent and normal vectors of the link are denoted, respectively, as $\mathbf{t}_i = \cos\theta_i\mathbf{e}_x + \sin\theta_i\mathbf{e}_y$ and $\mathbf{n}_i = \mathbf{e}_z \times \mathbf{t}_i$, where θ_i is the angle between the tangent vector $\mathbf{t}_i$ and the unit basis vector $\mathbf{e}_x$. Therefore, the position vector along the i-th link is given by $\mathbf{X}_i = \mathbf{x}_i + s\mathbf{t}_i$, where $s \in [0,\ell]$ is the arclength along the link. The discretization is subject to the kinematic constraints between successive links,

$$\mathbf{x}_{i+1} = \mathbf{x}_i + \ell\mathbf{t}_i = \mathbf{x}_i + [\ell\cos\theta_i, \ell\sin\theta_i]. \tag{2}$$

The hydrodynamic force on the i-th link is therefore given by

$$\mathbf{F}_i^h = \int_0^\ell \mathbf{f}^h(\mathbf{X}_i)\, \mathrm{d}s, \tag{3}$$

and the hydrodynamic torque on the i-th link about $\mathbf{x}_j$ is given by

$$\mathbf{T}_{i,j}^h = \int_0^\ell (\mathbf{X}_i - \mathbf{x}_j) \times \mathbf{f}^h(\mathbf{X}_i)\, \mathrm{d}s. \tag{4}$$

At low Reynolds numbers, the multi-link model satisfies the

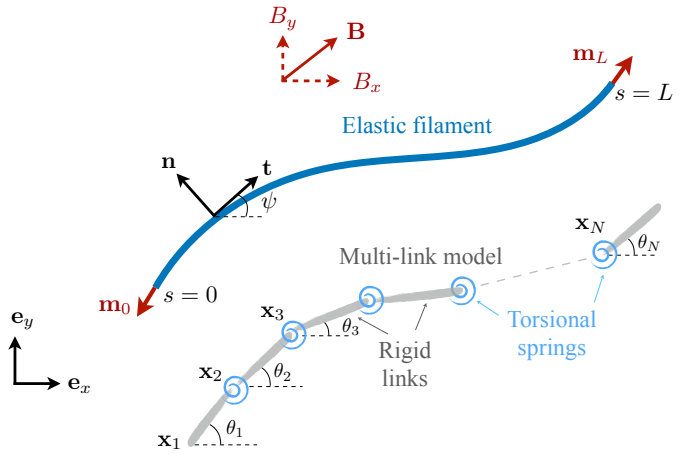

Fig. 2 Schematic diagram of an elastic filament with prescribed magnetic moments ($\mathbf{m}_0$ and $\mathbf{m}_L$) at its two ends under an oscillating external magnetic field $\mathbf{B}$. The elastic filament is discretized by a chain of rigid links connected by torsional springs.

overall balance of force

$$\sum_{i=1}^{N} \mathbf{F}_i^h = \mathbf{0}, \tag{5}$$

and torque

$$\sum_{i=1}^{N} \mathbf{T}_{i,1}^h + \mathbf{T}_0^m + \mathbf{T}_L^m = \mathbf{0}, \tag{6}$$

in addition to the torque balances on the assembly minus the n-th link ($n = 1, \ldots, N-1$)

$$\sum_{i=n+1}^{N} \mathbf{T}_{i,n+1}^h + \mathbf{T}_n^e + \mathbf{T}_L^m = \mathbf{0}. \tag{7}$$

Here the elastic torque by the torsional spring is given by

$$\mathbf{T}_n^e = -k(\theta_{n+1} - \theta_n)\mathbf{e}_z, \tag{8}$$

and $\mathbf{T}_0^m$ and $\mathbf{T}_L^m$, respectively, denote the magnetic torque at the left and right ends of the filament. To represent an elastic filament with bending stiffness A, the spring constant in the multi-link model can be adjusted as $k = AN/L$. The kinematic constraints between successive links (Eq. 2) together with the force and torque balances (Eqs. 5–7) form a system of first-order ordinary differential equations. To determine the unknown position vectors $\mathbf{x}_i$ and angles θ_i, the system of differential equations is integrated numerically with the initial condition of a straight filament oriented horizontally using the `MATLAB ode15s` solver.

We have validated the multi-link framework against results based on the continuum description of an elastic filament[36] (see Appendix A for more details). The results from the multi-link model with $N = 50$ display satisfactory agreement with the predictions based on the continuum description of an elastic filament as shown in Fig. 6 in the appendix. Hereafter we use $N = 100$ in all simulations in this work.

2.2 Magnetic actuation

To actuate the filament magnetically, we impose a typical spatially uniform external magnetic field $\mathbf{B} = b\mathbf{e}_x + b\sin\omega t\mathbf{e}_y$ considered in previous studies[17,32,41,52,53]: the field consists of a homogeneous static component of strength b in the $x-$direction and a sinusoidally oscillating field of amplitude b and frequency ω in the y-direction. The resulting magnetic field $\mathbf{B}$ thus oscillates around the $x-$axis by $\pm 45°$, with a magnitude that varies between b and $\sqrt{2}b$.

To model the filament driven by two magnets at the ends, we prescribe a magnetic moment $\mathbf{m}_L = m_L\mathbf{t}(s = L, t)$ of strength m_L at the right end and another magnetic moment $\mathbf{m}_0 = \pm m_0\mathbf{t}(s = 0, t)$ of strength m_0 at the left end (see Fig. 2). Here, the positive sign $(+)$ corresponds to the case where the two magnetic moments are of the same polarity, whereas the negative sign $(-)$ corresponds to the case where the two magnetic moments are of opposite polarity. The uniform external magnetic field exerts no net force, but magnetic torques given by $\mathbf{T}_L^m = \mathbf{m}_L \times \mathbf{B} = m_L b[\cos\theta_N \sin\omega t - \sin\theta_N]\mathbf{e}_z$ and $\mathbf{T}_0^m = \mathbf{m}_0 \times \mathbf{B} = \pm m_0 b[\cos\theta_1 \sin\omega t - \sin\theta_1]\mathbf{e}_z$ at the two ends of the filament.

2.3 Non-dimensionalization

We non-dimensionalize lengths by L, time by $1/\omega$, and forces by $L^2\xi_\perp\omega$ in this problem. Several relevant dimensionless groups emerge in the non-dimensionalization: the first group $\mathrm{Sp} = L(\xi_\perp\omega/A)^{1/4}$, referred to as the sperm number in the literature[17,19,33,54,55], compares the magnitudes of the viscous and elastic torques. Another dimensionless group, $\mathrm{Mn} = (m_0 + m_L)b/L^3\xi_\perp\omega$, a type of Mason number, compares the magnitudes of the magnetic and viscous torques. In this work, we consider a fixed total sum of magnetic strengths at the filament's two ends $(m_0 + m_L)$ and focus on the case when $\mathrm{Mn} = 1$ (*i.e.*, when the magnetic and viscous torques are comparable). We will examine the propulsion dynamics in this regime by varying the fraction of the magnetic strength at the left end ($s = 0$) of the filament, $\mathrm{M}_0 = m_0/(m_0 + m_L)$, where the limiting cases $M_0 = 0$ and $M_0 = 1$ reduce to the setup where the filament is driven at only one end considered in previous works[41,56]. We denote similarly the fraction $\mathrm{M}_L = 1 - \mathrm{M}_0 = m_L/(m_0 + m_L)$. Lastly, we employ a drag anisotropy ratio $\gamma = \xi_\perp/\xi_\parallel = 2$ in all simulations by considering the limiting case of a slender filament with $L/a \to \infty$. Hereafter, we consider only dimensionless quantities and use the same symbols as their dimensional counterparts for simplicity.

3 Results and Discussion

In this section, we examine the propulsion characteristics of the elastic filament as a function of the relative flexibility (Sp) and the magnetic strength fraction (M_0). To explore the design space, we consider magnetic moments with same polarity (§3.1) and opposite polarity (§3.2) at the two ends of the filament in the following subsections.

3.1 Magnetic moments with same polarity

We consider the propulsion of an elastic filament driven by magnetic moments of the same polarity at its two ends. We quantify

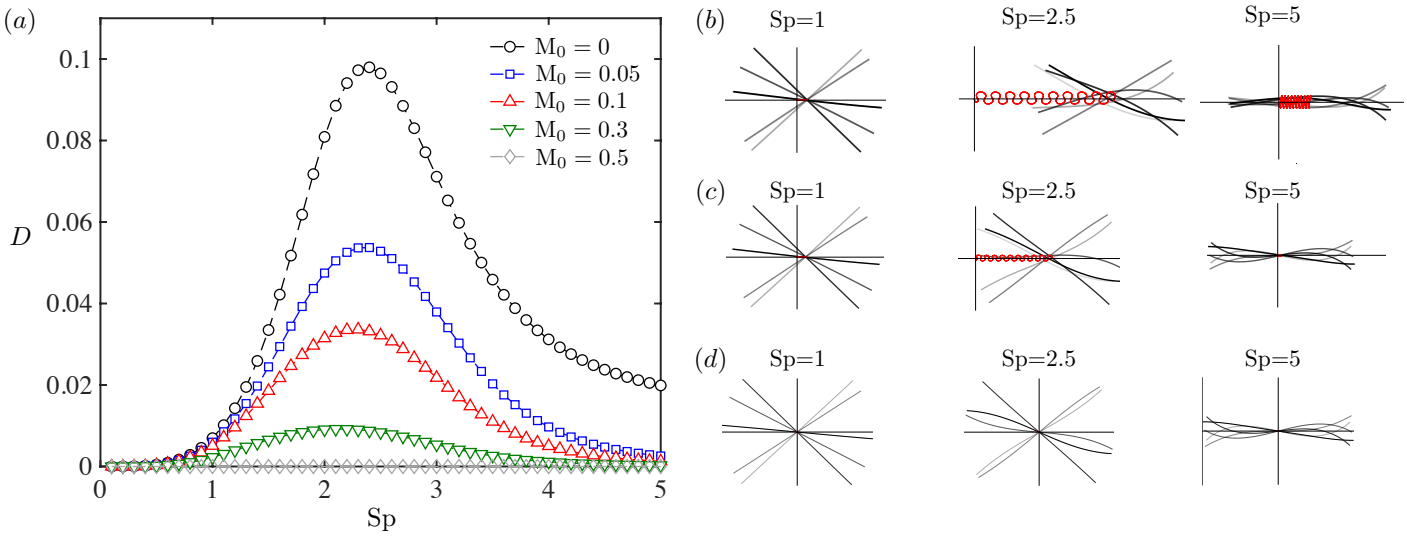

Fig. 3 Propulsion characteristics of the elastic filament with magnetic moments of same polarity. (a) The dimensionless displacement of the filament D in a single cycle as a function of the sperm number, Sp, at varying levels of relative magnetic strength M_0. Panels (b)–(d): the shape of the filament at different time instants in a cycle (the color of the filament turns from light to dark as time proceeds) at different Sp for (b) $M_0 = 0$, (c) $M_0 = 0.05$, and (d) $M_0 = 0.5$. Here the red lines display the trajectories of the mid-point of the filament from their initial positions represented by the vertical black lines over 10 cycles.

the propulsion performance of the filament by tracking the displacement of its midpoint ($s = 1/2$) in the $x-$direction over one period of magnetic actuation (T), *i.e.*, $D = x(s = 1/2, t+T) - x(s = 1/2, t)$. To diminish the initial transient effect, we report the displacement D after repeated periods of actuation when $t = 24T$. In Fig. 3(a), we display D as a function of the sperm number, Sp, for various magnetic configurations. As a benchmark, we first consider the limiting case of $M_0 = 0$ [black circles, Fig. 3(a)], which corresponds to the configuration of an elastic driven at only one end with $M_L = 1 - M_0 = 1$, similar to the setup considered in previous works[41,56]. At low Sp, the filament is relatively stiff with insignificant deformation [Fig. 3(b), Sp=1]. The largely straight filament hence undergoes a nearly reciprocal motion following the magnetic actuation, which leads to ineffective propulsion as constrained by Purcell's scallop theorem[14,57]. As Sp increases, the filament becomes more flexible, allowing the development of more shape deformations along the filament to escape the time-reversal symmetry in the sequence of motion for propulsion [Fig. 3(b), Sp=2.5]. The propulsion performance reaches a maximum at Sp ≈ 2.5, before decaying with further increase in Sp. At higher Sp, the deformation becomes more localized around the actuated end due to the increased flexibility of the filament [*e.g.*, see Fig. 3(b), Sp $= 5$], leading to less effective propulsion performance in this regime. See ESI Movie 1 for an animation of Fig. 3(b), $M_0 = 0$.

When a second magnetic moment with the same polarity is present at the left end, the propulsion of the filament exhibits qualitative features that are similar to the case where $M_0 = 0$, as shown in Fig. 3(a) for $M_0 = 0.05$ (blue squares), $M_0 = 0.1$ (red upward triangles), and $M_0 = 0.3$ (green downward triangles). However, the overall propulsion performance is reduced monotonically as the strength of the magnetic moment at the left end M_0 increases. We can understand this reduction in propulsion performance by considering the special case of $M_0 = 0.5$: since the magnetic moments are of the same strength and polarity, the anti-symmetry of such a magnetic arrangement produces shape deformations along the filament that are anti-symmetric about its midpoint [see Fig. 3(d) and the corresponding animation in ESI Movie 1]. Consequently, the left and right halves of the filament generate propulsive thrusts that are equal in magnitude but opposite in direction, leading to a net zero propulsion [Fig. 3(a), gray diamonds]. As M_0 increases from 0 to 0.5, the reduction in propulsion performance can therefore be attributed to the development of increasingly anti-symmetric deformations along the left half of the filament [see Fig. 3(c) and the corresponding animation in ESI Movie 1], which generates a growing propulsive thrust that counteracts the thrust due to the right half of the filament. The physical mechanism at play can be compared to a tug-of-war between the thrust generated by the magnetic actuation at the left and right ends of the filament. This results in the filament propelling in the direction of the stronger magnetic moment, but with a reduced net driving force.

As a remark, in the above discussion we focus on the cases with $M_0 \in [0, 0.5]$, where the filament always propels in the positive $x-$direction (to the right). For cases with $M_0 > 0.5$, for example $M_0 = 0.7$ and hence $M_L = 0.3$, such a configuration is equivalent to (with a flip between left and right) the configuration where $M_0 = 0.3$ and $M_L = 0.7$. The filaments therefore exhibit the same propulsion characteristics in these two cases but in opposite propulsion directions; *i.e.*, the filament with $M_0 = 0.7$ and $M_L = 0.3$ propels in the negative $x-$direction (to the left). See ESI Movie 3 for animations that compare these two cases. Thus, Fig. 3 provides a comprehensive illustration of the full range of propulsion dynamics for $M_0 \in [0, 1]$.

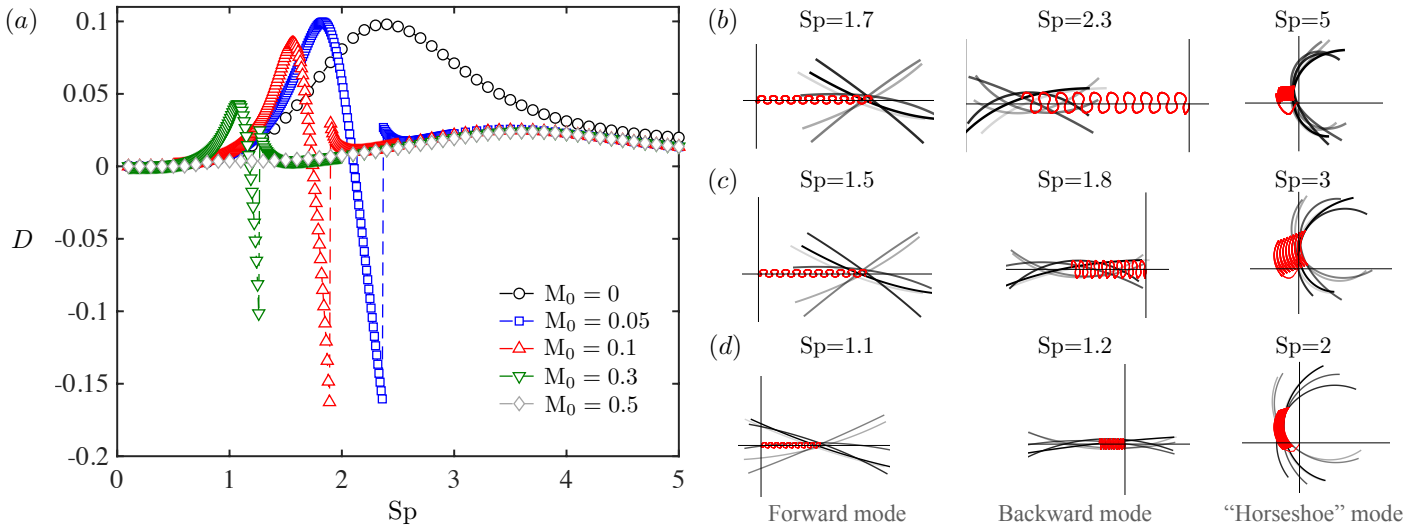

Fig. 4 Propulsion characteristics of the elastic filament with magnetic moments of opposite polarity. (a) The dimensionless displacement of the filament D in a single cycle as a function of the sperm number, Sp, at varying levels of relative magnetic strength M_0. Panels (b)–(d): the shape of the filament at different time instants in a cycle (the color of the filament turns from light to dark as time proceeds) at different Sp for (b) $M_0 = 0.05$, (c) $M_0 = 0.1$, and (d) $M_0 = 0.3$. Here the red lines display the trajectories of the mid-point of the filament from their initial positions represented by the vertical black lines over 10 cycles.

3.2 Magnetic moments with opposite polarity

We now examine the propulsion of an elastic filament driven by magnetic moments of opposite polarity at its two ends. In Fig. 4(a), the filament displacement D for the case of a single magnetic moment ($M_0 = 0$) is displayed again as a benchmark (black circles). Unlike the scenario discussed in §3.1 where the magnetic moments have the same polarity, adding a second magnetic moment with opposite polarity ($M_0 > 0$) results in a qualitative change in the filament's propulsion behavior. New modes of propulsion emerge depending on the value of Sp as shown in Fig. 4(a). For a given magnetic moment $0 < M_0 < 0.5$, the filament first exhibits the forward propulsion mode at small Sp, where it propels in the positive $x-$direction (forward) in a manner similar to that observed in §3.1. As Sp increases beyond the forward-mode regime, the filament then transitions into a new mode of motion referred to as the backward mode, where the filament propels in the negative $x-$direction (backward). A further increase in Sp brings about the "horseshoe" mode, where the filament bends into a "C" or "horseshoe" shape. We discuss these individual modes of motion in more detail below.

(i) Forward mode: For a given value of $M_0 < 0.5$ (*e.g.*, $M_0 = 0.05$, 0.1, and 0.3 in Fig. 4), the propulsion behavior in the small Sp regime is qualitatively similar to the case with the same polarity: As Sp goes to zero, the net displacement of the filament vanishes as a result of the increasingly stiff filament undergoing reciprocal motion. As Sp increases from zero, the flexibility of the filament enables it to propel in the positive $x-$direction. In contrast to the scenario when the magnetic moments have the same polarity, where the optimal values of Sp for propulsion occur around 2.5 for different values of M_0 [Fig. 3(a)], the Sp that maximizes forward propulsion in the case of opposite polarity depends sensitively on the value of M_0, occurring at $Sp \approx 2$ for $M_0 = 0.05$ (blue squares) and $Sp \approx 1$ for $M_0 = 0.3$ (green downward triangles). Although the case of $M_0 = 0.05$ shows a slight enhancement in D at the optimal Sp compared to the case of $M_0 = 0$, the propulsion performance deteriorates with higher values of M_0. Furthermore, the regime of Sp for forward propulsion reduces in size as M_0 increases and disappears entirely when $M_0 = 0.5$, where the filament only exhibits the "horseshoe" mode (see more discussion below). The shapes and trajectory of the filament undergoing forward propulsion are displayed in Figs. 4(b) $Sp = 1.7$, 4(c) $Sp = 1.5$, and 4(d) $Sp = 1.1$. See also ESI Movie 2 for the corresponding animations.

(ii) Backward mode: As a new feature unique to the case of magnetic moments of opposite polarity, the filament inverts its propulsion direction from forward to backward (negative $x-$direction) as Sp increases as depicted in Fig. 4(a). The shapes and trajectory of the filament exhibiting this backward propulsion mode are displayed in Figs. 4(b) $Sp = 2.3$, 4(c) $Sp = 1.8$, and 4(d) $Sp = 1.2$. See also ESI Movie 2 for the corresponding animations. The backward propulsion emerges as a result of an intricate interplay between filament flexibility and the opposite magnetic actuation of the filament at its two ends. When a magnetic moment of opposite polarity is added to the left end of the filament, its orientation is significantly different from that of the external magnetic field. Even if the magnetic moment is of a low strength (small M_0), the drastic orientation difference generates relatively large torques and thus deformations at the filament's left end when Sp is sufficiently large, driving the propulsion of the filament toward the left (negative $x-$direction). A stronger magnetic moment M_0 further increases the magnitude of the torque at the filament's left end and thereby enables the occurrence of backward propulsion at a smaller Sp (a relatively stiffer filament) as shown in Fig. 4(a). We also note that for a given value of M_0, although backward

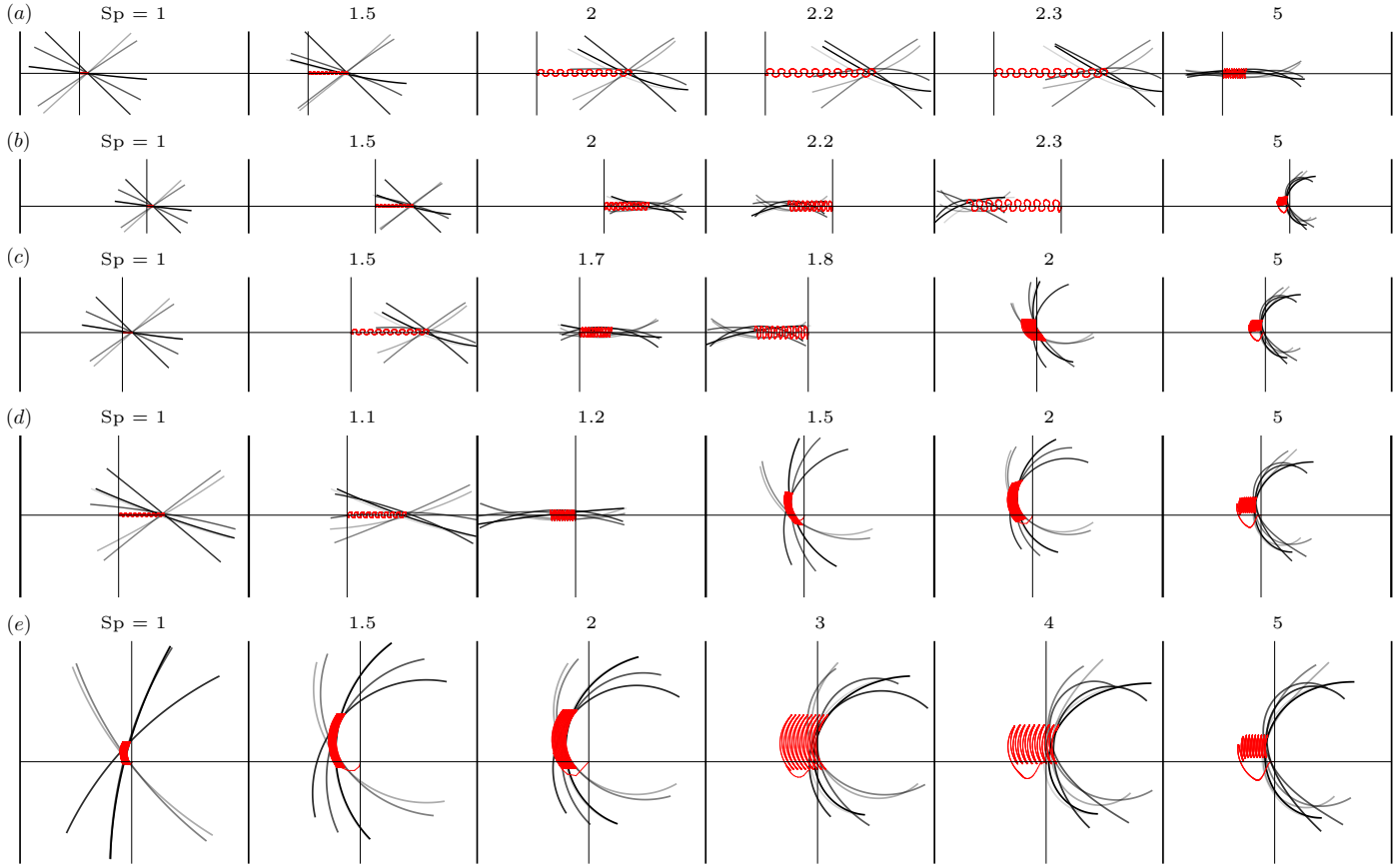

Fig. 5 Deformation of the filament with magnetic moments of opposite polarity. The shape of the filament at different time instants in a cycle (the color of the filament turns from light to dark as time proceeds) at different Sp for (a) $M_0 = 0$, (b) $M_0 = 0.05$, (c) $M_0 = 0.1$, (d) $M_0 = 0.3$, and (e) $M_0 = 0.5$. Here the red lines display the trajectories of the mid-point of the filament from their initial positions represented by the vertical black lines over 10 cycles.

propulsion only occurs within a relatively small regime of Sp, the filament can propel more effectively [a larger displacement per period D as shown in Fig. 4(a)] in the backward mode than in the forward mode. Compared to the maximum possible displacement generated by a single magnetic moment ($D \approx 0.1$ for $M_0 = 0$), the addition of a magnetic moment with opposite polarity enables the filament to produce approximately 50% more displacement in the backward mode ($D \approx -0.15$ for $M_0 = 0.05$ and $M_0 = 0.1$).

(iii) "Horseshoe" mode: As Sp increases beyond the backward mode regime, the filament transitions into another new mode of motion (referred to as the "horseshoe" mode) with only small positive displacements, as shown in Fig. 4(a). In this "horseshoe" mode, the relative flexibility of the filament increases to the point where the magnetic moment at its left end can drive it to bend significantly into a "horseshoe" shape so that both magnetic moments largely align with the external magnetic field, as shown in Figs. 4(b) Sp = 5, 4(c) Sp = 3, and 4(d) Sp = 2. See ESI Movie 2 for the corresponding animations. These "horseshoes" rock back and forth in response to the oscillating external magnetic field, giving rise to ineffective but non-zero propulsion in the positive $x-$direction for different values of M_0 as shown in Fig. 4(a). When $M_0 = 0.5$, the magnetic moment becomes strong enough to drive the significant re-orientation of the left end of the filament, which is necessary for inducing the "horseshoe" mode, even when the filament is relatively stiff. The filament hence only undergoes the "horseshoe" mode in the full range of Sp shown in Fig. 4(a) with minimal positive displacements, without exhibiting the forward and backward propulsion modes described above.

As a remark, similar to the case for magnetic moments of the same polarity, here we focus on the results for $M_0 \in [0, 0.5]$. When $M_0 > 0.5$, for example $M_0 = 0.7$ and hence $M_L = 0.3$, due to the larger magnetic moment at the left end of the filament, the filament will initially re-orient itself by rotating close to 180° so that the larger magnetic moment aligns more favorably with the external magnetic field. The re-orientation process causes the left and right sides of the filament to switch positions, resulting in the same magnetic configuration and hence the same propulsion behavior as the case of $M_0 = 0.3$ and $M_L = 0.7$ depicted in Fig. 4(a). See ESI Movie 4 for animations that illustrate the initial re-orientation process and compare the propulsion behavior in these two cases. In other words, apart from the initial re-orientation process, the propulsion characteristics of configurations with $M_0 = c > 0.5$ are essentially identical to those of their corresponding cases with $M_0 = 1 - c < 0.5$.

Fig. 5 presents an overview of the propulsion behavior of the filament with magnetic moments with opposite polarity at its two ends. To summarize, only a single mode of propulsion is observed for the limiting cases of $M_0 = 0$ (the forward mode) and $M_0 = 0.5$ (the "horseshoe" mode). For other magnetic strengths $0 < M_0 < 0.5$, as the filament becomes relatively more flexible (increasing Sp), it undergoes a transition from the forward mode to the backward mode and ultimately to the "horseshoe" mode. Among these modes of propulsion, the backward mode can generate the most filament displacement in one period, while the "horseshoe" mode is the least effective in terms of the magnitude of propulsion.

4 Concluding Remarks

In this work, we investigated the propulsion characteristics of an elastic filament driven by magnetic moments at its two ends. To explore the design space, we examined filaments with varying relative stiffness, as well as magnetic moments with different polarities and magnitudes. Compared to a filament driven by a single magnetic moment at one end, our results show that adding a magnetic moment of the same polarity does not alter the qualitative propulsion behavior, but consistently reduces propulsion magnitude as the strength of the added magnetic moment increases. In stark contrast, adding a magnetic moment of the opposite polarity leads to the emergence of previously unobserved modes of elastohydrodynamic propulsion at different regimes of Sp, referred to as the forward, backward, and "horseshoe" modes. In particular, the filament in the backward mode can generate the largest magnitude of propulsion unattainable by a single magnetic moment alone. These findings could guide the development of soft microrobots that can propel more effectively and perform more complex maneuvers (e.g., bi-directional propulsion) by modulating the magnetic actuation (*e.g.*, the magnetic strength and actuation frequency) and/or the effective bending stiffness of the flexible structure.

The idealized problem setup enables us to rationalize the elastohydrodynamic behavior of the filament by unraveling the complex interplay between the viscous and elastic forces with the magnetic actuation in different configurations. We remark on several limitations resulting from the idealizations, which indicate possible avenues for future investigations. First, in this work we limit our consideration to point magnetic torques and ignore any hydrodynamic influences from the magnetic materials used in experimental realization. As a simplifying assumption, this approach provides a reasonable approximation when the magnetic materials' size is small compared to the characteristic lengths in the setup. We also assumed a spatially uniform external magnetic field in this work, while permanent magnets with dipolar fields may be used in experiments[26,46]. In the latter case, the propulsion performance of the elastic filament may also depend on its proximity to the actuating permanent magnet. Future studies should examine how spatially varying magnetic fields impact the propulsion performance of elastic swimmers. Second, here, we model the hydrodynamics of the filament using the resistive force theory, a local drag model that assumes negligible non-local hydrodynamic interactions between different parts of the filament when they are sufficiently well separated. However, for more complex geometries where parts of the body come into close proximity, a non-local slender body theory[58,59] is required to accurately capture the dynamics. Third, our investigation has focused on the case when the Mason number is equal to unity, where the sum of the magnetic torques are comparable to viscous torques, and uncovered some interesting new propulsion behaviors in this specific regime. A more comprehensive study characterizing the dynamics in different regimes of the Mason number should be pursued in future work. Finally, we consider a Newtonian fluid medium in this work, while many biological fluids display complex (non-Newtonian) rheology including viscoelasticity and shear-thinning viscosity[60–62]. Further investigation into how different non-Newtonian rheological behaviors impact the propulsion of the two-magnet configuration considered here could offer valuable insights for future biomedical applications of soft microswimmers.

Conflicts of interest

There are no conflicts to declare.

Acknowledgements

This work was supported by the National Science Foundation under grant number 1830958.

A Validation of the multi-link model

In this appendix, we validate the multi-link model by comparing its numerical results against results based on a continuum description of the elastic filament reported in a previous asymptotic analysis[36]. We consider an elastic filament undergoing a harmonic oscillation at one of its ends as $y(0,t) = \varepsilon \sin t$, where ε is the dimensionless oscillation amplitude. The average propulsive thrust (in $x-$direction) generated by the boundary actuation can be calculated by integrating the hydrodynamic force along the filament, $F_p = -\left\langle \mathbf{e}_x \cdot \int_0^1 \mathbf{f}^h \, \mathrm{d}s \right\rangle$, where the angle brackets denote time averaging over a period of actuation. For small amplitude oscillations ($\varepsilon \ll 1$), the propulsive thrust can be expanded asymptotically in ε as $F_p \sim \varepsilon^2 F_p^{(2)} + O(\varepsilon^4)$, because the odd powers vanish by the $\varepsilon \to -\varepsilon$ symmetry. The leading-order propulsive thrust can be calculated asymptotically from the filament shape (we refer interested readers to the mathematical details in Ref.[36]) and the results are shown in Fig. 6 (black solid line) as a function of Sp. We use the multi-link model described in §2.1 with $N = 50$ to generate the corresponding numerical results (blue circles), which display satisfactory agreements with the asymptotic results based on a continuum description of the elastic filament.

Notes and references

1 B. J. Nelson, I. K. Kaliakatsos and J. J. Abbott, *Annu. Rev. Biomed. Eng.*, 2010, **12**, 55–85.

2 M. Sitti, H. Ceylan, W. Hu, J. Giltinan, M. Turan, S. Yim and E. Diller, *Proc. IEEE Inst. Electr. Electron. Eng.*, 2015, **103**, 205–224.

3 Z. Wu, Y. Chen, D. Mukasa, O. S. Pak and W. Gao, *Chem. Soc. Rev.*, 2020, **49**, 8088–8112.

4 J. J. Abbott, K. E. Peyer, M. Cosentino Lagomarsino, L. Zhang,

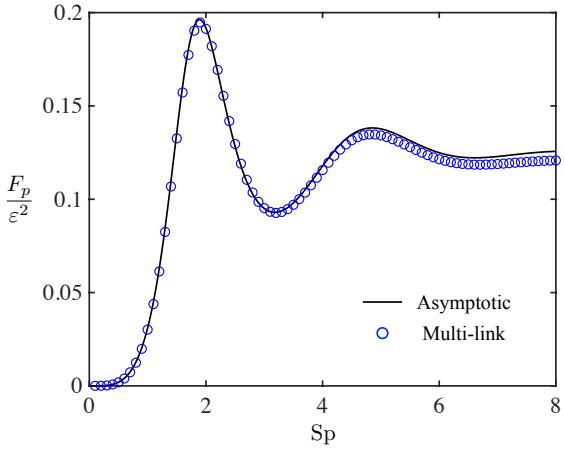

Fig. 6 The propulsive thrust F_p/ε^2 generated by an elastic filament oscillated harmonically at one end as a function of the sperm number Sp with $\varepsilon = 0.1$. Numerical results from the multi-link model with $N = 50$ (blue circles) display satisfactory agreements with previous asymptotic results based on a continuum description of the elastic filament[36] (black solid line).

L. Dong, I. K. Kaliakatsos and B. J. Nelson, *Int. J. Robot. Res.*, 2009, **28**, 1434–1447.

5 S. J. Ebbens and J. R. Howse, *Soft Matter*, 2010, **6**, 726–738.

6 E. Diller and M. Sitti, *Found. Trends Robot.*, 2013, **2**, 143–259.

7 J. L. Moran and J. D. Posner, *Annu. Rev. Fluid Mech.*, 2017, **49**, 511–540.

8 C. Hu, S. Pané and B. J. Nelson, *Annu. Rev. Control Robot. Auton. Syst.*, 2018, **1**, 53–75.

9 M. Sitti, *Nat. Rev. Mater.*, 2018, **3**, 74–75.

10 L. J. Fauci and R. Dillon, *Annu. Rev. Fluid Mech.*, 2006, **38**, 371–394.

11 E. Lauga and T. R. Powers, *Rep. Prog. Phys.*, 2009, **72**, 096601.

12 J. M. Yeomans, D. O. Pushkin and H. Shum, *Eur. Phys. J. Spec. Top.*, 2014, **223**, 1771–1785.

13 J. Elgeti, R. G. Winkler and G. Gompper, *Rep. Prog. Phys.*, 2015, **78**, 056601.

14 E. M. Purcell, *Am. J. Phys.*, 1977, **45**, 3–11.

15 S. Camalet and F. Jülicher, *New J. Phys.*, 2000, **2**, 24.

16 I. H. Riedel-Kruse, A. Hilfinger, J. Howard and F. Jülicher, *HFSP Journal*, 2007, **1**, 192–208.

17 R. Dreyfus, J. Baudry, M. L. Roper, M. Fermigier, H. A. Stone and J. Bibette, *Nature*, 2005, **437**, 862–865.

18 W. Gao, S. Sattayasamitsathit, K. M. Manesh, D. Weihs and J. Wang, *J. Am. Chem. Soc.*, 2010, **132**, 14403–14405.

19 O. S. Pak, W. Gao, J. Wang and E. Lauga, *Soft Matter*, 2011, **7**, 8169–8181.

20 I. S. M. Khalil, H. C. Dijkslag, L. Abelmann and S. Misra, *Appl. Phys. Lett.*, 2014, **104**, 223701.

21 I. S. M. Khalil, A. Fatih Tabak, A. Klingner and M. Sitti, *Appl. Phys. Lett.*, 2016, **109**, 033701.

22 S. H. Kim, S. Hashi and K. Ishiyama, *IEEE Trans. Magn.*, 2011, **47**, 3244–3247.

23 E. Diller, J. Zhuang, G. Zhan Lum, M. R. Edwards and M. Sitti, *Appl. Phys. Lett.*, 2014, **104**, 174101.

24 W. Hu, G. Z. Lum, M. Mastrangeli and M. Sitti, *Nature*, 2018, **554**, 81–85.

25 T. Xu, J. Zhang, M. Salehizadeh, O. Onaizah and E. Diller, *Sci. Robot.*, 2019, **4**, eaav4494.

26 L. N. Pham, J. A. Steiner, K. K. Leang and J. J. Abbott, *IEEE Trans. Med. Robot.*, 2020, **2**, 598–607.

27 C. H. Wiggins and R. E. Goldstein, *Phys. Rev. Lett.*, 1998, **80**, 3879–3882.

28 C. H. Wiggins, D. Riveline, A. Ott and R. E. Goldstein, *Biophys. J.*, 1998, **74**, 1043 – 1060.

29 M. Lagomarsino, F. Capuani and C. Lowe, *J. Theor. Biol.*, 2003, **224**, 215–224.

30 T. S. Yu, E. Lauga and A. E. Hosoi, *Phys. Fluids*, 2006, **18**, 091701.

31 E. Lauga, *Phys. Rev. E*, 2007, **75**, 041916.

32 M. Roper, R. Dreyfus, J. Baudry, M. Fermigier, J. Bibette and H. A. Stone, *Proc. R. Soc. A*, 2008, **464**, 877–904.

33 E. E. Keaveny and M. R. Maxey, *J. Fluid Mech.*, 2008, **598**, 293–319.

34 H. Gadêlha, *Regul. Chaot. Dyn.*, 2013, **18**, 75–84.

35 A. M. Maier, C. Weig, P. Oswald, E. Frey, P. Fischer and T. Liedl, *Nano Lett.*, 2016, **16**, 906–910.

36 Z. Peng, G. J. Elfring and O. S. Pak, *Soft Matter*, 2017, **13**, 2339–2347.

37 Z. Liu, F. Qin and L. Zhu, *Phys. Rev. Fluids*, 2020, **5**, 124101.

38 Z. Liu, F. Qin, L. Zhu, R. Yang and X. Luo, *Phys. Fluids*, 2020, **32**, 041902.

39 J. Espinosa-Garcia, E. Lauga and R. Zenit, *Phys. Fluids*, 2013, **25**, 031701.

40 B. Thomases and R. D. Guy, *Phys. Rev. Lett.*, 2014, **113**, 098102.

41 K. Qin, Z. Peng, Y. Chen, H. Nganguia, L. Zhu and O. S. Pak, *Soft Matter*, 2021, **17**, 3829–3839.

42 R. F. Ausas, C. G. Gebhardt and G. C. Buscaglia, *Commun. Nonlinear Sci. Numer. Simul.*, 2022, **108**, 106213.

43 T. S. Singh, P. Singh and R. D. S. Yadava, *Soft Matter*, 2018, **14**, 7748–7758.

44 S. Hu, J. Zhang and M. J. Shelley, *Soft Matter*, 2022, **18**, 3605–3612.

45 S. Lim, A. Yadunandan and M. Khalid Jawed, *Soft Matter*, 2023, –.

46 J. A. Steiner, L. N. Pham, J. J. Abbott and K. K. Leang, *J. Mech. Robot.*, 2022, **14**, 051002.

47 J. Gray and G. J. Hancock, *J. Exp. Biol.*, 1955, **32**, 802–814.

48 J. Lighthill, *Mathematical Biofluiddynamics*, SIAM, Philadelphia, 1975.

49 F. Alouges, A. DeSimone, L. Giraldi and M. Zoppello, *Int. J. Nonlin. Mech.*, 2013, **56**, 132 – 141.

50 F. Alouges, A. DeSimone, L. Giraldi and M. Zoppello, *Soft Robot.*, 2015, **2**, 117–128.

51 C. Moreau, L. Giraldi and H. Gadêlha, *J. R. Soc. Interface*,

2018, **15**, 20180235.
52 K. E. Peyer, L. Zhang and B. J. Nelson, *Nanoscale*, 2013, **5**, 1259–1272.
53 E. Gutman and Y. Or, *Phys. Rev. E*, 2014, **90**, 013012.
54 C. P. Lowe, *Phil. Trans. R. Soc. B*, 2003, **358**, 1543–1550.
55 H. Gadêlha, E. A. Gaffney, D. J. Smith and J. C. Kirkman-Brown, *J. R. Soc. Interface*, 2010, **7**, 1689–1697.
56 O. S. Pak, W. Gao, J. Wang and E. Lauga, *Soft Matter*, 2011, **7**, 8169–8181.
57 S. Childress, *Mechanics of swimming and flying*, Cambridge University Press, 1981.
58 R. E. Johnson, *J. Fluid Mech.*, 1980, **99**, 411–431.
59 A.-K. Tornberg and M. J. Shelley, *J. Comput. Phys*, 2004, **196**, 8–40.
60 J. Sznitman and P. E. Arratia, *Complex Fluids in Biological Systems*, Springer New York, 2015, pp. 245–281.
61 G. J. Elfring and E. Lauga, *Complex Fluids in Biological Systems*, Springer New York, 2015, pp. 283–317.
62 S. E. Spagnolie and P. T. Underhill, *Annu. Rev. Condens. Matter Phys.*, 2023, **14**, null.